NOSC

NOSC TR 238

NOSC TR 238

Technical Report 238

ELECTRO-OPTICAL DETECTION OF URANIUM-238 DECAY PRODUCTS IN THE ATMOSPHERE

LIDAR remote sensing techniques are studied to determine effectiveness in detecting uranium ore

JE Solomon
17 February 1978

Final Report: February 1976 - January 1978

Prepared for
U.S. Department of Energy
Grand Junction Office
Grand Junction, Colorado

NAVAL OCEAN SYSTEMS CENTER
SAN DIEGO, CALIFORNIA 92152

NAVAL OCEAN SYSTEMS CENTER, SAN DIEGO, CA 92152

AN ACTIVITY OF THE NAVAL MATERIAL COMMAND

RR GAVAZZI, CAPT, USN
Commander

HL BLOOD
Technical Director

ADMINISTRATIVE INFORMATION

The work reported in this document was performed at NOSC for the US Department of Energy, Grand Junction Office, under agreement number E(05-1)-1672.

Released by
EJ Wesley, Head
Radiation Physics Division

Under authority of
HR Talkington, Head
Ocean Technology Department

(9) final rept. Feb 76-Jan 78

UNCLASSIFIED

SECURITY CLASSIFICATION OF THIS PAGE *(When Data Entered)*

REPORT DOCUMENTATION PAGE		READ INSTRUCTIONS BEFORE COMPLETING FORM
(14) 1. REPORT NUMBER NOSC-TR-238	2. GOVT ACCESSION NO.	3. RECIPIENT'S CATALOG NUMBER
(6) 4. TITLE *(and Subtitle)* ELECTRO-OPTICAL DETECTION OF URANIUM-238 DECAY PRODUCTS IN THE ATMOSPHERE, LIDAR remote sensing techniques are studied to determine effectiveness in detecting uranium ore,		5. TYPE OF REPORT & PERIOD COVERED Final Report – Feb 1976-Jan 1978 6. PERFORMING ORG. REPORT NUMBER
7. AUTHOR(s) (10) JE Solomon		8. CONTRACT OR GRANT NUMBER(s)
9. PERFORMING ORGANIZATION NAME AND ADDRESS Naval Ocean Systems Center San Diego, CA 92152		10. PROGRAM ELEMENT, PROJECT, TASK AREA & WORK UNIT NUMBERS E(05-1) 1672
11. CONTROLLING OFFICE NAME AND ADDRESS U.S. Department of Energy Grand Junction Office Grand Junction, CO	(11)	12. REPORT DATE 17 February 1978 13. NUMBER OF PAGES 22 (12) 25 p.
14. MONITORING AGENCY NAME & ADDRESS *(if different from Controlling Office)*		15. SECURITY CLASS. *(of this report)* UNCLASSIFIED 15a. DECLASSIFICATION/DOWNGRADING SCHEDULE

16. DISTRIBUTION STATEMENT *(of this Report)*

Approved for public release; distribution unlimited

17. DISTRIBUTION STATEMENT *(of the abstract entered in Block 20, if different from Report)*

18. SUPPLEMENTARY NOTES

19. KEY WORDS *(Continue on reverse side if necessary and identify by block number)*

electrooptics, optical detection, actinide series compounds

20. ABSTRACT *(Continue on reverse side if necessary and identify by block number)*

This study was conducted in two phases. The first phase dealt with theoretical calculations of expected detection sensitivities using LIDAR remote sensing techniques to measure airborne daughter products of ^{238}U. The most promising species for this technique were found to be ^{214}Bi and ^{210}Pb, with effective photon scattering cross sections of 3.5×10^{-17} cm^2 and 8×10^{-15} cm^2 respectively. The theoretical calculations regarding system sensitivity were based on approximate calculations of the appropriate transition probabilities and estimates of the effects of atmospheric fluorescent quenching. Phase two consisted of experimental measurements of the total effective photon scattering cross sections and the effects of quenching by various atmospheric gases. Results of

DD FORM 1 JAN 73 1473 EDITION OF 1 NOV 65 IS OBSOLETE
S/N 0102-014-6601

UNCLASSIFIED
SECURITY CLASSIFICATION OF THIS PAGE *(When Data Entered)*

8 tons 10 to the -13/4 power 50 cm

39515

20. Continued.

these measurements indicated that the calculated transition probabilities and effective scattering cross sections, exclusive of quenching, were in reasonable agreement with measured values. However, results of the quenching measurements showed that the original theoretical estimates had underestimated the effects of quenching by more than an order of magnitude. Calculations of expected LIDAR system performance based on the experimentally measured quantities showed that, although the system would be very sensitive by normal standards (1 part in 10^{18} at a range of 180 m), it would still be inadequate to the needs of an aerial survey search for ^{238}U ore deposits.

CONTENTS

INTRODUCTION

The study described in this technical report was undertaken to ascertain the feasibility of remote optical detection of ^{238}U daughter products in the atmosphere. The technique, if practical, would provide an alternative to the current gamma-spectroscopy systems used in aerial searches for underground uranium deposits. The investigation consisted of two phases. In Phase I a theoretical examination of the detection problem was undertaken to determine the approximate sensitivity to be expected from a pulsed-laser remote (airborne) detection system. These calculations yielded very encouraging figures for the over-all performance of such a system. However, the calculations required the use of several estimates of physical quantities whose values could not be calculated with any degree of accuracy. In particular, estimates of atmospheric quenching processes were thought to be very uncertain. Phase II of this study concentrated on laboratory measurements of the important physical parameters that had been either approximated or simply estimated in the Phase I calculations.

PHASE ONE

BACKGROUND

Recent progress in the field of remote detection, by laser probing techniques, has demonstrated the feasibility of long-range detection of low-concentration species in the atmosphere[1,2,3]. The current study was undertaken to determine the feasibility of these techniques, as applied to the problem of detecting very low concentrations of ^{238}U daughter products in the atmosphere. In particular, we were interested in determining the usefulness of these laser techniques as a means of background removal in aerial gamma-ray spectroscopic searches for uranium ore deposits. Current aerial survey techniques use the gamma spectrum of ^{214}Bi as an indication of possible uranium ore deposits; however, the rather large "background" due to airborne ^{214}Bi between the survey craft and the ground severely limits the sensitivity of this method.

Since the airborne ^{214}Bi comes from the decay of atmospheric ^{222}Rn, it was believed that an optical technique for the detection of radon would provide a means for the removal of the airborne ^{214}Bi background. Laser probe techniques generally rely on the absorption of photons at the laser wavelength (λ_L) by the target species and subsequent remission of photons at a different wavelength (λ_e). The process is shown schematically in figure 1. The condition that the target species reradiate, at a wavelength different from the laser wavelength, is required so that the detection system be able to discriminate against atmospheric Rayleigh and Mie scattering. Furthermore, the relative transition probabilities for transitions b-a and b-c should be such that, once excited to the b-state, there is a reasonably high probability that the atom will decay by the b-c channel rather than the b-a. These

1. Solomon, JE and Silva, DM, "Detection of N_2^+ Produced by Ionizing Radiation in the Atmosphere", NUC TN-1497, NOSC (Jan. 1975); Solomon, JE and Silva, DM, J. Appl. Phys., No. 47 (1976), p. 1519.
2. Schuler, CJ; Pike, CT and Miranda, HA, Appl. Optics, No. 10 (1971), p. 1689.
3. Hirschfeld, T; Schildkrant, ER; Tannenbaum, H; and Tannenbaum, D; Appl. Phys. Lett., No. 22 (1973), p. 38.

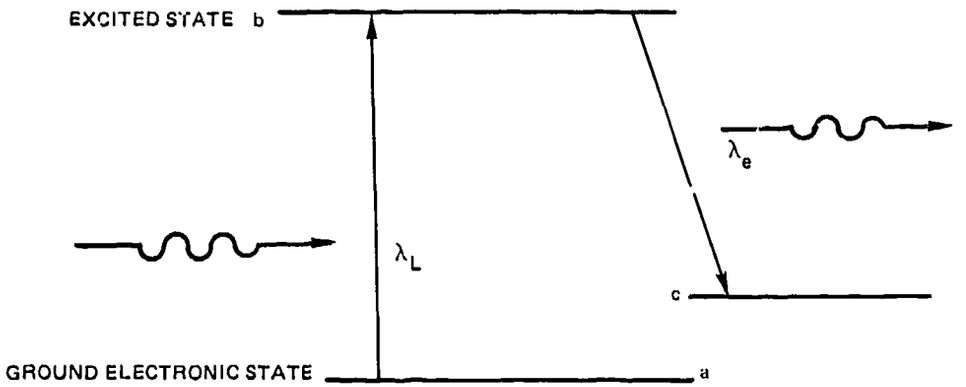

Figure 1. General three-level system illustrating the laser-probe detection scheme.

requirements impose rather severe constraints on the atomic species which are detectable by laser probe methods.

We show in figure 2 simplified energy level diagrams of the three numbers of the ^{222}Rn decay sequence, which are the most likely choices as "target" species for a laser probe measurement system. As can be seen immediately, radon is a particularly poor choice; since one must observe at the same wavelength as the laser probe. In addition to

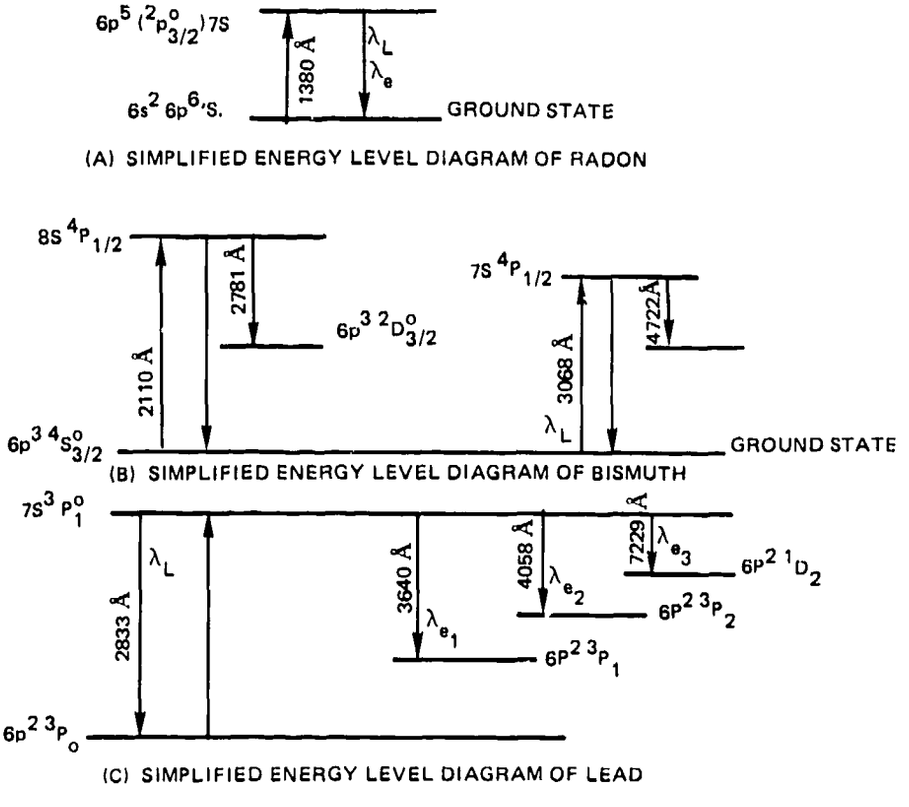

Figure 2. Energy level diagrams.

this drawback, the probing wavelength has an extremely high atmospheric attenuation coefficient, due to oxygen continuum absorption in this region of the spectrum. We are thus left with ^{214}Bi and ^{210}Pb as possible candidates for a laser probe detection system. Therefore, Phase One concentrated on an evaluation of the feasibility of using an optical detection scheme for background removal, based on laser probe detection of either ^{214}Bi or ^{210}Pb.

TRANSITION PROBABILITIES IN BISMUTH AND LEAD

A major problem in evaluating the useful sensitivity attainable, in the application of laser probe techniques to a specific atomic or molecular system, arises in the determination of the relevant transition probabilities. For the problem at hand, we require a knowledge of the transition probabilities of the following transitions in bismuth and lead:

Bi: $6p^2 7s\ ^4P_{1/2} - 6p^3\ ^4S^o_{3/2}$

$6p^2 7s\ ^4P_{1/2} - 6p^3\ ^2D^o_{3/2}$

Pb: $6p7s\ ^3P^o_1 - 6p^2\ ^3P_o$

$6p7s\ ^3p^o_1 - 6p^2\ ^3P_1$

$6p7s\ ^3p^o_1 - 6p^2\ ^3P_2$

$6p7s\ ^3p^o_1 - 6p^2\ ^1D_2$

An extensive literature search was conducted, both manually and with the assistance of a computer-based data-search system, for previously published results on these particular transitions. The results are summarized in Table 1. The values entered in the table represent the most probable value based on the available literature.

The results of our literature survey indicate that very little work has been done on the bismuth system; in fact, we found essentially no theoretical work on the transitions of interest in Bi. For the transitions in Pb, the first three entries are taken from measured values of the appropriate oscillator strengths and are probably correct to within ten percent. The value given for the $6p7s\ ^3P^o_1 - 6p^2\ ^1D_2$ transitions is from an intermediate coupling calculation, which yielded rather poor agreement with absolute measurements on the other transitions.

TABLE 1. TRANSITION PROBABILITIES.

Element	Transition	λ(Å)	$A_{jk}(sec^{-1})$	Ref.
Bi	$7s\ ^4P_{1/2} - 6p^3\ ^4S^o_{3/2}$	3068	1.7×10^8	(4) (5)
	$7s\ ^4P_{1/2} - 6p^3\ ^2D^o_{3/2}$	4722		
Pb	$7s\ ^3P^o_1 - 6p^2\ ^3P_o$	2833	1.7×10^8	(6) (7) (8)
	$7s\ ^3P^o_1 - 6p^2\ ^3P_1$	3640	1.16×10^8	(6) (7) (8)
	$7s\ ^3P^o_1 - 6p^2\ ^3P_2$	4058	3.72×10^8	(6) (7) (8)
	$7s\ ^3P^o_1 - 6p^2\ ^1D_2$	7229	4.1×10^5 (?)	(8)

In general, the transition probability (or transition rate) may be expressed as[9]

$$A(\alpha'J',\alpha J) = \frac{2.026 \times 10^{18}}{g(J')\,\lambda 3}\ S(\alpha'J',\alpha J), \tag{1}$$

where the primed quantities refer to the initial level. The quantity $g(J')$ is the statistical weight of the upper level and λ is the transition wavelength expressed in angstrom units. The quantity denoted by $S(\alpha'J',\alpha J)$ is the line strength factor for the transition $\alpha'J' \rightarrow \alpha J$, and may be factored as follows[9,10]:

$$S(\alpha'J',\alpha J) = S(M)S(L)\sigma^2, \tag{2}$$

where S(M) is the factor depending on the particular multiplet considered and S(L) is a factor which depends on the particular line within the multiplet. Both S(M) and S(L) may be determined from angular-momentum coupling considerations[11,12]. The quantity σ^2 is related to the electric-dipole transition integral as

$$\sigma^2 = \frac{1}{(4\ell^2 - 1)}\left(\int_0^\infty R_{n'\ell'}\, R_{n\ell} r dr\right) \tag{3}$$

4. Cunningham, PT and Link, JK, J. Opt. Soc. Amer., No. 57, (1967), p. 1000.
5. Svanberg, S, Phys. Ser., No. 5, (1972), p. 73.
6. Gibbs, HM, Churchill GG, and Salamo EJ, Phys. Rev. A., No. 7, (1973), p. 1766.
7. DeZabra, RL and Marshall, Alan, Phys. Rev., No. 170, (1968), p. 28.
8. Lawrence, GM, Astrophys. J., No. 148, (1967), p. 261.
9. Bates, DR and Damgaard, A, Phil. Trans. A, No. 101 (1949).
10. Seaton, MJ, Royl. Astron. Soc. MN, No. 118, (1958), p. 504; Burgess, A and Seaton, MJ, Royl. Astron. Soc. MN, No. 120, (1960), p. 121.
11. Shore, BW and Menzel, DH; Principles of Atomic Spectra, John Wiley and Sons, N.Y., 1968.
12. Condon, EV and Shortley, GH, The Theory of Atomic Spectra, Cambridge Univ. Press, 1964, n. pag.

where the $R_{n\ell}$'s refer to the radial wave functions of the upper and lower states of the transition. Bates and Damgaard give an extensive tabulation of values of σ^2 which they calculated on the basis of a central-field Coulomb approximation. For simple one-electron systems, this approximation is quite good. Even in more complex systems, with more than one electron outside a closed shell, it gives surprisingly good results. The first three of the transitions in Pb listed in Table 1 have been calculated using the Bates and Damgaard procedures, as well as by intermediate coupling schemes (DeZabra, Lawrence). Of course, the $3p_1^o - {}^1D_2$ transition must be evaluated in an intermediate coupling scheme, since the transition is forbidden in both LS and jj coupling representations.

The evaluation of transition probabilities in both lead and bismuth is further complicated by the existence of configuration interaction. Examination of the energy levels of the two atoms shows that configuration interaction is probably more pronounced in the case of Bi than in Pb. Instead of attempting a full scale intermediate-coupling calculation, with configuration interaction to evaluate the transition probability for the $({}^4P_{1/2} - {}^2D^o_{3/2})$ Bi transition, it is probably more reasonable to make a simple estimate based on the roughly analogous transition in Pb. Consideration of the measured relative oscillator strengths in Pb (Gibbs, DeZabra) and the calculations of Lawrence lead one to the conclusion that a reasonable estimate for the ratio A(7229)/A(2833) in the lead is $\sim 6 \times 10^{-3}$; where A(7229) is the transition probability for the $(7s\,{}^3P_1^o - 6p^2\,{}^1D_2)$ transition and A(2833) is the transition probability for the $(7s\,{}^3P_1^o - 6p^2\,{}^3P_o)$ transition. Since configuration interaction is probably stronger in the case of Bi, we will take 2×10^{-2} as an estimate of A(4711/A(3068) in Bi. With the above considerations in mind, we have taken the values shown in Table 2 as our estimate of the relevant transition probabilities in Bi and Pb.

TABLE 2.

Element	Transition (j - k)	λ(Å)	$A_{jk}(\text{sec}^{-1})$	B^r_{jk}
Bi	$7s^4P_{1/2} - 6p^3\,{}^4S^o_{3/2}$	3068	1.7×10^8	0.98
	$7s^4P_{1/2} - 6p^3\,{}^2D^o_{3/2}$	4722	3.4×10^6	0.02
Pb	$7s^3P_1^o - 6p^2\,{}^3P_o$	2833	1.7×10^8	0.26
	$7s^3P_1^o - 6p^2\,{}^3P_1$	3640	1.16×10^8	0.17
	$7s^3P_1^o - 6p^2\,{}^3P_2$	4058	3.72×10^8	0.56
	$7s^3P_1^o - 6p^2\,{}^1D_2$	7229	1.04×10^6	0.002

In table 2 we have also listed the resulting branching ratio B^r_{jk}, defined by

$$B^r_{jk} \equiv \frac{A_{jk}}{\sum_{\substack{\ell \\ \ell < j}} A_{j\ell}} \qquad (4)$$

An alternative set of transition arrays in bismuth and lead are shown in figures 3 and 4. Very little hard data exists on these particular transitions, although oscillator

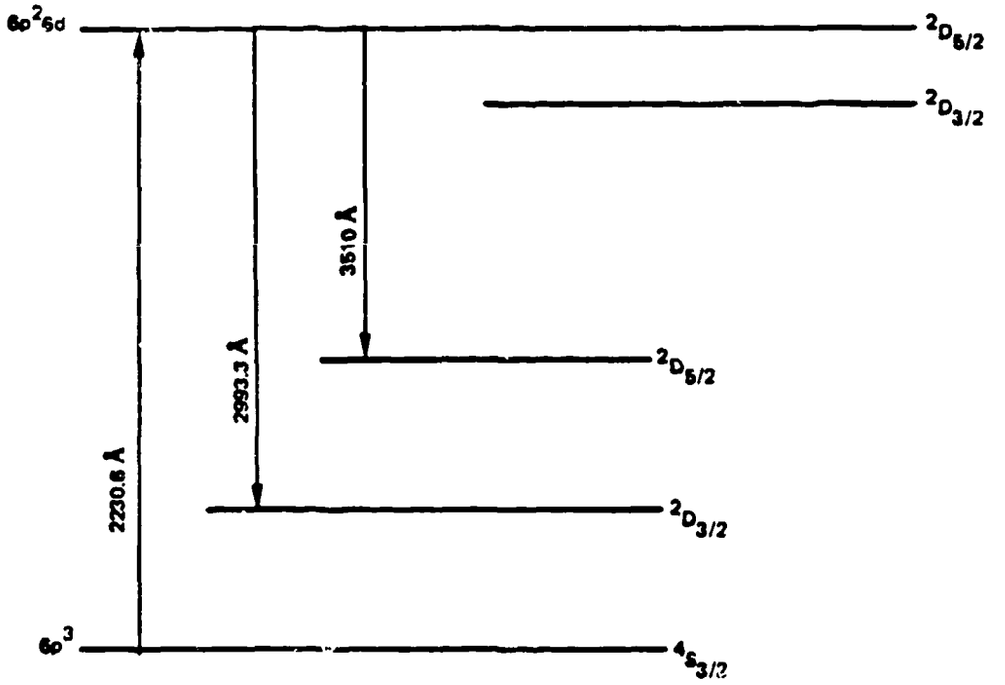

Figure 3. Alternate transition array in atomic bismuth.

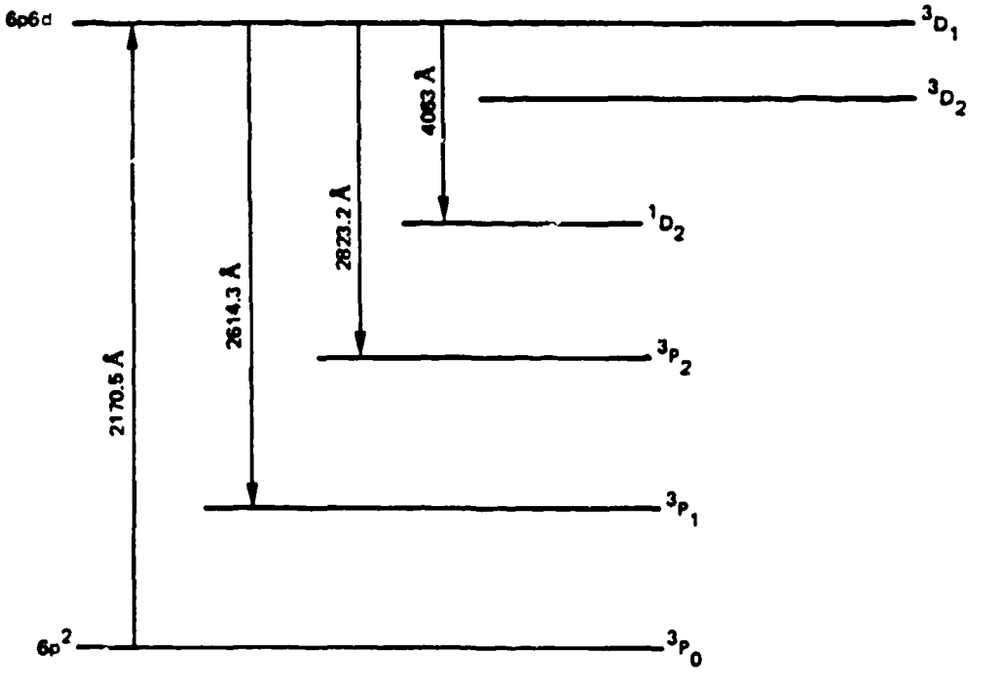

Figure 4. Alternate transition array in atomic lead.

strengths for the two resonance absorptions in this set of transition arrays are cited by Kirkbright and Sargent[13]. Using the coulomb approximation, we have calculated the transitions probabilities for the set of transitions shown in figures 3 and 4, and the results are collected in Table 3. An indication of the reliability of these calculations is the fact that the transition probability calculated for the $6p6d(^3D_1) - 6p^2(^3P_o)$ transition in lead agrees to within about 10% of the value obtained from the measured oscillator strength cited by Kirkbright and Sargent.

TABLE 3.

Element	Transition (*j* - *k*)	λ(Å)	$A_{jk}(sec^{-1})$	B^r_{jk}
Bi	$6p^26d(^2D_{5/2}) - 6p^3(^4S_{3/2})$	2230.6	1.07×10^7	0.11
	$6p^26d(^2D_{5/2}) - 6p^3(^2D_{3/2})$	2993.3	7.09×10^6	0.07
	$6p^26d(^2D_{5/2}) - 6p^3(^2D_{5/2})$	3510	7.98×10^7	0.82
Pb	$6p6d(^3D_1) - 6p^2(^3P_o)$	2170.5	2.14×10^8	0.67
	$6p6d(^3D_1) - 6p^2(^3P_1)$	2614.3	1.06×10^8	0.33
	$6p6d(^3D_1) - 6p^2(^3P_2)$	2832.2	7.98×10^6	–

DETECTABILITY LEVELS

The number of photons per laser pulse detected by our system as a result of probing an extended source may be written as

$$\phi_d = 1.2 \times 10^{24} \times \frac{A_d}{r^2} \sigma_{jk\ell}\, \eta_o\, E_L\, \lambda_L\, \tau\, [X]\, T_\lambda \qquad (5)$$

where A_d = collector area in m^2,

r = mean "target" range in meters,

$\sigma_{jk\ell}$ = effective cross section (cm^2) for absorption at laser wavelength λ_L, and subsequent remission at wavelength λ_d,

η_o = optical detection efficiency including photomultiplier,

E_L = laser energy in joules,

λ_L = laser wavelength in Å,

τ = laser pulse width in sec,

T_λ = atmospheric transmission factor,

$[X]$ = "target" species concentration in cm^{-3}.

13. Kirkbright, GF and Sargent, M, Atomic Absorption and Fluorescence Spectroscopy (Academic Press, NY, 1974), n. pag.

The atmospheric transmission factor for both incident laser beam and return signal may be written as

$$T_\lambda = e^{-(\alpha_L + \alpha_d)r}, \tag{6}$$

where α_L is the attenuation coefficient at the laser wavelength and α_d is the attenuation coefficient at the return signal wavelength; both are units of m^{-1}. We may thus write the number of return signal photons per laser pulse as

$$\phi_d = 1.2 \times 10^{24} \frac{A_d}{r^2} \sigma_{jk\ell}\, \eta_o\, E_L\, \lambda_L\, \tau\, [X]\, e^{-(\alpha_L + \alpha_d)r}. \tag{7}$$

The effective cross section $\sigma_{jk\ell}$, may be calculated from a knowledge of the absorption cross section σ_{jk}, the branching ratio $B_{k\ell}$, and the relative fluorescence efficiency $F^r_{k\ell}$.

The appropriate expression (Solomon and Silva) is

$$\sigma_{jk\ell} = F^r_{k\ell}\, B^r_{k\ell}\, \sigma_{jk}. \tag{8}$$

The relative fluorescence efficiency is a measure of the probability that the upper state (here denoted by k) will be quenched by collisions. The branching ratio simply indicates the probability that the upper state will radiatively decay via the $k \rightarrow \ell$ channel. We now proceed to evaluate each of the factors appearing in equation (8).

THE ABSORPTION CROSS SECTION

The frequency-dependent cross section for absorption may be written as

$$\phi_{jk(\omega)} = \frac{3\pi c^2 A_{jk}}{\omega_o^2} \quad \frac{\Gamma/2\pi}{(\omega - \omega_o)^2 + \Gamma^{2/4}}, \tag{9}$$

where ω_o is the angular frequency of the absorption line center, and Γ is the absorption line width also in units of angular frequency. In order to obtain the integrated absorption cross section we may use the relation

$$\sigma_{jk} = \int \sigma_{jk}(\omega)\, g(\omega)\, d\omega, \tag{10}$$

where $g(\omega)$ is the normalized spectral profile of the pumping source (i.e., the laser), and assuming a Lorentzian profile of width λ_L for our laser source, equation (10) may be evaluated immediately. The result is

$$\sigma_{jk} = \frac{3\, c^2}{\omega_o^2} \cdot \frac{A_{jk}}{\Gamma + \gamma_L}. \tag{11}$$

FLUORESCENCE EFFICIENCIES

At atmospheric pressure, collisional deactivation of the excited atomic state competes strongly with radioactive decay. The relative fluorescence efficiency $F^r_{k\ell}$, may be expressed in terms of natural lifetime $\tau^o_{k\ell}$ and the apparent lifetime $\tau_{k\ell}$, at pressure p. The relative fluorescence efficiency is thus given by

$$F^r_{k\ell} = \frac{\tau_{k\ell}}{\tau^o_{k\ell}} \quad . \tag{12}$$

Assuming predominately two-body collisional deactivation, the quenching process may then be described by a general Stern-Volmer relation as

$$F^r_{k\ell} = \frac{\tau_{k\ell}}{\tau^o_{k\ell}} = \left[1 + \frac{p(M_1)}{p'(M_1)} + \ldots + \frac{p(M_n)}{p'(M_n)} \right]^{-1} \quad , \tag{13}$$

where $p(M_i)$ is the partial pressure of the i-th quenching species and $p'(M_i)$ is the "critical quenching" pressure of the i-th species. The critical quenching pressure may be related to the quenching cross section by[14]

$$\frac{1}{p'(M_i)} = \tau^o_{k\ell}\, \sigma_{k\ell}\,(M_i) N \tilde{\nu} \quad , \tag{14}$$

where $\sigma_{k\ell}\,(M_i)$ is the cross section for quenching of the $k \rightarrow \ell$ transition by species M_i; N is the number density of particles at 1 torr (3.26×10^{16} cm^{-3}); and $\tilde{\nu}$ is the relative velocity of the collision partners.

For the case of the $^3P^o_1$ level of Pb, Gibbs[15] finds a quenching cross section with N_2 of 1.6×10^{-15} cm^2. No data appear to be available for quenching by O_2; and there appear to be no data available at all for quenching levels in Bi. Assuming the quenching cross section O_2 to be at least comparable to that of N_2, using equations (14) and (13) we find the relative fluorescence efficiencies for transitions from the $^3P^o_1$ state in Pb to be:

$$F^r_{3640} = 0.046$$

$$F^r_{4058} = 0.133$$

$$F^r_{7229} = 4 \times 10^{-4}$$

There is presently no data available on the quenching cross section for the 6p6d $^3D_1$ level of lead. However, one would expect that the cross section would be of the same order as for the $^3P^o_1$ level. Assuming this to be the case, we find:

$$F^r_{2614} = 0.043$$

$$F^r_{2823} = 0.0033$$

14. O'Neil, R and Davidson, G, Air Force Cambridge Research Laboratories Report, AFCRL-67-0277 (1967), n. pag.
15. Gibbs, HM, Phys. Rev. A, No. 5 (1972), p. 2408.

Although there are no published quenching cross sections for the $^4P_{1/2}$ level in Bi, it is likely that these cross sections are at least as great as those for the $^3P_1^o$ level in Pb. In fact, the cross section for quenching by 0_2 may be significantly larger due to the existence of two levels in 0_2 ($C\ ^3\Delta_u$ and $A\ ^3\Sigma_u^+$), which are almost energy resonant with the $7s\ ^3P_1^o$ level of Bi. Assuming this to be the case, and choosing quenching cross sections as follows:

$$\sigma_{k\ell}(N_2) = 1.6 \times 10^{-15}\ cm^2$$

$$\sigma_{k\ell}(0_2) = 1.6 \times 10^{-14}\ cm^2$$

we find for the 4722 Å transition in Bi:

$$F^r_{4722} = 7 \times 10^{-4}$$

For the $6p^26d(^2D_{5/2})$ level of bismuth we will assume a quenching cross section comparable to that of lead, since there appear to be no resonance quenchers in air for this level. Under this assumption we then find:

$$F^r_{2993} = 0.003$$

$$F^r_{3510} = 0.032$$

Proceeding with our evaluation of detectable levels of Bi and Pb, we now require an estimate of the quantities Γ and γ_L appearing in equation (11). The quantity Γ is the absorption line width at atmospheric pressure and a reasonable estimate is $\Gamma \sim 10^9\ sec^{-1}$ (angular frequency). The laser spectral width may reasonably be taken as $\gamma_L \sim 10^{11}\ sec^{-1}$ (angular frequency). Using these values we have calculated the absorption cross sections σ_{jk}, for the 2833 Å transition in Pb and the 3068 Å transition in Bi. These quantities are then used to calculate the effective cross section $\sigma_{jk\ell}$, for the various possible detection channels. The results of our calculations are collected in Table 4, where λ_L denotes the laser wavelength and λ_d denotes the receiving wavelength.

TABLE 4.

Element	λ_L(Å)	λ_d(Å)	$\sigma_{jk}(cm^2)$	$B^r_{k\ell}$	$F^r_{k\ell}$	$\sigma_{jk\ell}(cm^2)$
Bi	3068	4722	1.05×10^{-13}	.02	7×10^{-4}	1.47×10^{-18}
	2240	2993	1.35×10^{-15}	.07	.033	2.84×10^{-19}
		3510	1.35×10^{-15}	.82	.032	3.54×10^{-17}
Pb	2833	3640	1.08×10^{-13}	.17	.046	8.45×10^{-16}
		4058	1.08×10^{-13}	.56	.133	8×10^{-15}
		7229	1.08×10^{-13}	.002	4×10^{-4}	8.64×10^{-20}
	2170	2614	7.65×10^{-14}	.33	.043	1.09×10^{-15}
		2823	7.65×10^{-14}	.025	.0033	6.31×10^{-18}

Returning to our expression for the number of detected return photons per laser pulse, equation (7),

$$\phi_d = 1.2 \times 10^{24} \frac{A_d}{r^2} \sigma_{jk\ell} \eta_o E_L \lambda_L \tau [X] e^{-(\alpha_L + \alpha_d)r} \quad (15)$$

we must now make some assumptions regarding an operational system. The appropriate atmospheric attenuation coefficients, α_L and α_d, depend strongly on wavelength in the regions under consideration, and the values used in what follows are taken from Koller[16]. The optical collection system is assumed to consist of short-focus, rhodium-flashed parabolic mirror, with an effective collection aperture of ~1 m^2. The total optical detection efficiency η_o is taken to be .06. The laser source is taken to be 1 joule per pulse with a pulse width of 200 ns. With these considerations in mind, we have collected in Table 5 the number of detected return photons per laser shot (at a range of 185 m), for each of the processes under consideration.

TABLE 5.

Element	λ_L(Å)	λ_d(Å)	ϕd
Bi	3068	4722	3.1×10^{-2} [Bi]
	2230	2993	1.5×10^{-3} [Bi]
		3510	0.19 [Bi]
Pb	2833	3640	16 [Pb]
		4058	148 [Pb]
		7229	1.6×10^{-3} [Pb]
	2170	2614	5.66 [Pb]
		2823	3.28×10^{-2} [Pb]

OPERATIONAL CONSIDERATIONS

Throughout the calculations of Transition Probabilities and Detectability Levels, we have attempted to consistently make conservative estimates of those quantities which have either not been measured, or are not amenable to accurate calculation. In the case of the transition probabilities, the agreement between the coulomb approximation calculations and measured values (where available) encourages one to believe that the calculated transition probabilities are not in error by more than 30% or so. The assumptions made with regard to quenching cross sections, for the various levels considered, may possibly be in error by as much as an order of magnitude (except in the one case of lead where measured value is available). The actual effects of quenching should probably be experimentally verified. The atmospheric attenuation coefficients used in calculating ϕ_d for Table 5 are average values,

16. Koller, LR, Ultraviolet Radiation, John Wiley and Sons, NY, 1965, p. 191.

for a visibility range of 20 km (12.4 mi), and these values tend to vary considerably depending on local atmospheric conditions (particularly dust and aerosol content).

REFLECTED SKY BACKGROUND

Operationally, our LIDAR system is viewing an extended background source of photons due to reflected skylight from the ground, and we must assess the effect of this background on our sensitivity. The number of background photons detected per laser pulse may be written as

$$\phi_b = \frac{A_s A_d}{r^2} \Delta\lambda \, N\lambda \, \eta_o \, \tau \tag{16}$$

where $\Delta\lambda$ is the spectral width of the optical system, A_s is the area of ground viewed, N_λ is the background spectral radiance (photons/sec/m^2/str/Å); and the other quantities are as defined previously. Figure 5 shows the solar spectral irradiance at sea level in the range of 2900 to 4000 Å[17]. As can be seen from the figure, the sky background falls quite dramatically at wavelengths shorter than ~3000 Å. In estimating the effective background spectral radiance we will assume, as worst case, a reflectivity of 10% for earth and vegetation; though it is likely to be much lower than this, particularly at shorter wavelengths. Then we have

$$N_\lambda = \rho \frac{H_\lambda}{\pi} \tag{17}$$

where ρ is the reflectivity, H_λ is the solar spectral irradiance (photons/sec/m^2/Å).

Signal processing, as applied to the laser probe system, involves subtracting the observed background from the background-plus-signal and co-adding the results of this process on successive laser shots. If we denote by ϕ_{sb} the number of background-plus-signal photons per laser shot, then

$$\phi_d = \phi_{sb} - \phi_b$$

is the number of detected signal photons per laser shot. The signal-to-noise ratio (SNR) for this detection process will be given by

$$(\text{SNR}) = \frac{\phi_d}{\sqrt{\phi_d + \phi_b}} \sqrt{n} \tag{18}$$

where n is the number of laser shots over which the data is accumulated. We see from equation (18) that, for situations where $\phi_b >> \phi_d$, the SNR varies directly with ϕ_d; while in the reverse case, $\phi_d >> \phi_b$, the SNR is proportional to $\sqrt{\phi_d}$. Table 6 shows values ϕ_d, ϕ_b, and SNR for the detection transitions treated in this report.

17. Smithsonian Physical Tables, (n.p., nd.), p. 723.

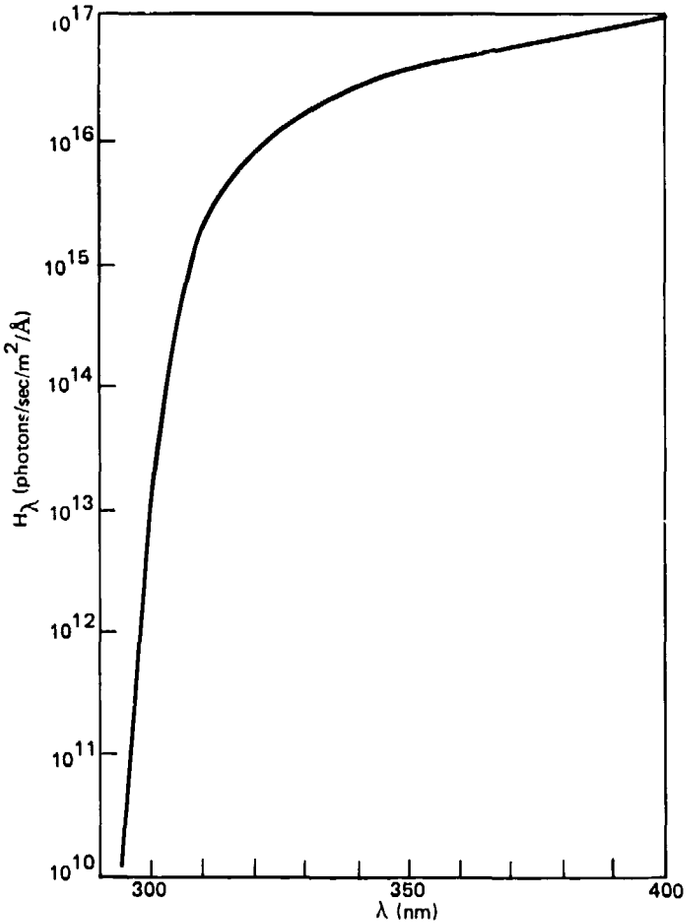

Figure 5. Solar spectral irradiance at the earth's surface. Taken from data published in reference 16.

TABLE 5.

Element	λ_L(Å)	λ_d(Å)	ϕ_d	ϕ_b	SNR
Bi	3068	4722	.031 [Bi]	3.2×10^4	$1.7 \times 10^{-4} \sqrt{n}$ [Bi]
	2230	2993	.0015 [Bi]	1.35	$1.3 \times 10^{-3} \sqrt{n}$ [Bi]
		3510	.19 [Bi]	3674	$3.1 \times 10^{-3} \sqrt{n}$ [Bi]
Pb	2833	3640	16. [Pb]	4684	$.2 \sqrt{n}$ [Pb]
		4058	148. [Pb]	1.5×10^4	$1.44 \sqrt{n}$ [Pb]
		7229	.0016 [Pb]	5×10^4	$7.2 \times 10^{-6} \sqrt{n}$ [Pb]
	2170	2614	5.66 [Pb]	<.003	$2.4 \sqrt{n}$ [Pb]
		2823	.033 [Pb]	<.003	$.2 \sqrt{n}$ [Pb]

AIRBORNE BISMUTH AND LEAD CONCENTRATIONS

In order to evaluate the possible usefulness of a LIDAR detection system based on the above calculations, we need to estimate the expected background concentrations of atomic ^{214}Bi and ^{210}Pb due to atmospheric ^{222}Rn. For the purposes of this calculation we take 1 pc/ℓ as the airborne background activity due to ^{222}Rn. Table 7 shows the expected, steady concentrations of the relevant decay products from ^{222}Rn, for a radon activity of 1 pc/ℓ, together with the expected SNR at that concentration for the most sensitive transition array in the particular element. Note, that in the case of ^{210}Pb, the natural half-life is 6.1×10^8 sec; however, one does not expect it to remain atomic lead for that long since it will eventually chemically combine with other species. The concentration of ^{210} Pb shown in the table is for an "effective" half-life of one hour. The value for the expected SNR shown in the table is expressed in terms of $\sqrt{n}$, the square root of the number of laser shots over which a single sample is accumulated.

TABLE 7.

Element	$\tau_{1/2}$ (sec)	Concentration	SNR
Radon $^{222}Rn_{86}$	3.5×10^5	20	–
Polonium $^{218}Po_{84}$	1.8×10^2	.011	–
Lead $^{214}Pb_{82}$	1.6×10^3	.098	$.75\sqrt{n}$
Bismuth $^{214}Bi_{83}$	1.2×10^3	.074	$9.6 \times 10^{-5}\sqrt{n}$
Polonium $^{214}Po_{84}$	1.6×10^{-4}	9.9×10^{-9}	–
Lead $^{210}Pb_{82}$	3600	.2	$1.1\sqrt{n}$

In order to visualize the capabilities of the proposed LIDAR system, we show the projected system operating characteristics in figures 6 and 7. The operating characteristics were calculated on the basis of the parameters shown in Table 5, with the additional constraints of a range increment of 15 m, and summation over 100 laser shots. The projected performance characteristics show quite clearly that lead is the "target specie" of choice, for a system designed to measure the concentrations of airborne decay products of ^{222}Rn.

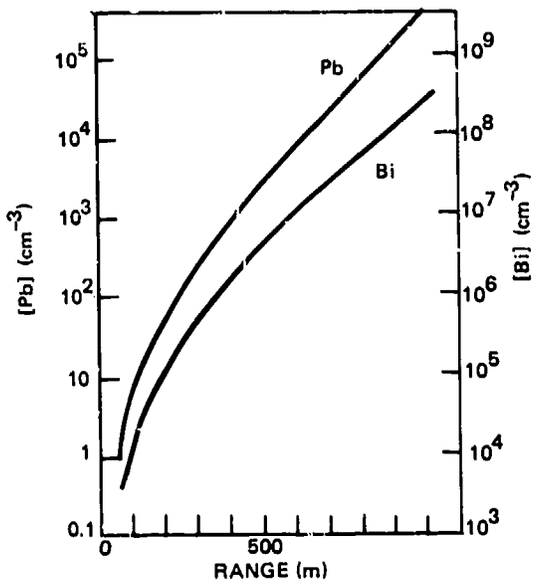

Figure 6. Theoretical lead and bismuth detectability levels vs range for a SNR of 10 and integration over 100 laser shots.

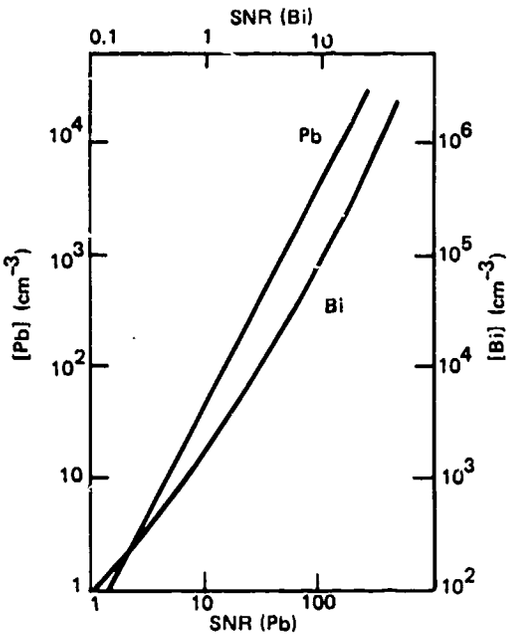

Figure 7. System performance characteristics at a range of 200 m and integration over 100 laser shots.

PHASE TWO

BACKGROUND

In order to test the validity of the assumptions made and calculations performed in Phase One, a series of laboratory measurements were carried out on pure lead vapor. These experiments were designed to measure the total effective scattering cross section in the pure lead system and the effects of quenching by N_2. Due to the elevated temperatures used to produce the lead vapors, it was not possible to measure quenching effects of oxygen.

EFFECTIVE SCATTERING CROSS-SECTIONS IN PURE LEAD VAPOR

The experimental set-up for this measurement is illustrated in figure 8. The lead scattering cell was constructed of suprasil quartz, 25 mm in diameter and 76 mm long. A lead reservoir was attached to the cell by a 5 mm length of 1 mm capillary tubing; and the cell was connected to the vacuum pumping system by a 5 mm long 1 mm capillary, terminated in a magnetically actuated quartz ball valve. The scattering cell and reservoir are enclosed in an oven which consists of two independent heaters (one for the cell and one for the lead reservoir). The scattering cell temperature was maintained at least 150°C higher than the reservoir temperature, to minimize condensation of lead vapor in the cell.

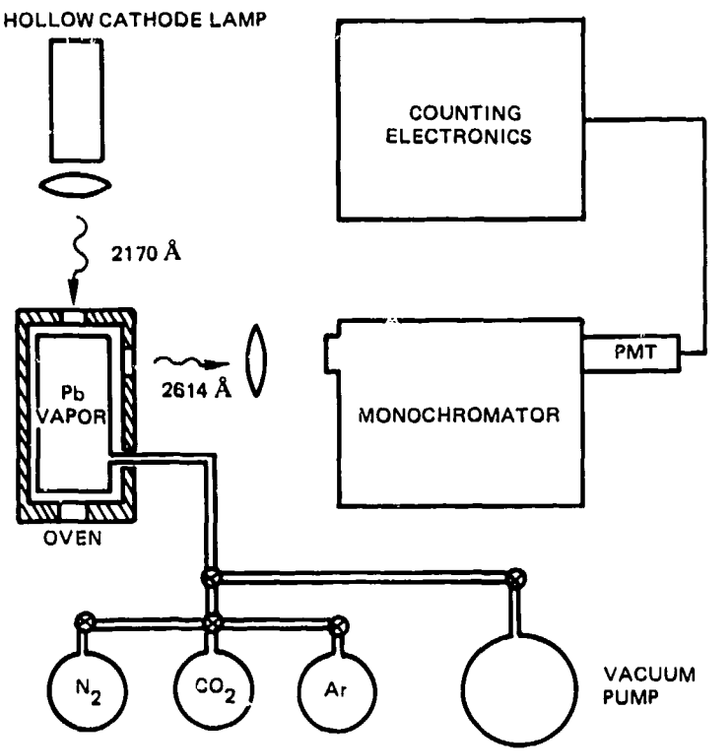

Figure 8. Block diagram of experimental measurement set-up.

The system was operated typically at a cell temperature of 920°C, and reservoir temperatures of from 400°to 500°C. These conditions corresponded to a range of lead vapor densities in the scattering cell of from about 2×10^{10} cm^{-3} to 5×10^{12} cm^{-3}. The system temperatures were continuously monitored with chromel-alumel thermocouples and a digital voltmeter.

The source of 2170 Å radiation was a highly modified Barnes Engineering, "Glomax" hollow cathode, lead lamp. This lamp provided a very intense source of both 2170 Å and 2833 Å lead resonance radiation. The lamp was operated with flowing helium at about 5 torr as the buffer gas, and lamp currents of 40 to 90 mA were used during the course of these measurements.

The scattered radiation was spectrally analyzed using Spex Industries 1/4 metre, double monochromator in second-order. The second-order spectral resolution was typically 5 Å. The output of the monochromator was detected using an EMI G-26H215, ultraviolet photomultiplier tube, and an Ortec photon-counting system. The photon-counting system was interfaced to the monochromator drive, and spectral data on the scattered radiation was acquired in 1 Å steps, with 50 second count periods. During spectral scans, the temperatures of the cell and reservoir were held constant to ±2.5°C.

Absolute spectral intensities were determined by calibration of the detector system and hollow cathode lamp, against a quartzphalogen standard of spectral irradiance. The absolute number density of scatters in the cell was determined from the temperatures of the cell and reservoir, together with the vapor pressure vs temperature data for lead. The absolute accuracy for measurement of spectral intensities was 10%, while that for determination of number densities was about 15%.

The cross section for scattering may be related to the experimentally measured quantities through the apparent source radiant emittance,

$$M_s = \frac{\langle n_s \rangle}{\eta U} \quad \text{(photons/cm}^2\text{/sec)}, \tag{19}$$

where η = total optical detection efficiency

U = collection system e'tendue

$\langle n_s \rangle$ = mean detected signal counts

The expression for the total effective scattering cross section is now given by

$$\sigma_{jk\ell} = \frac{M_s}{[Pb]\, I_o \ell} \quad (cm^2) \tag{20}$$

where $[Pb]$ = lead density (cm^{-3})

I_o = incident source intensity (photons/cm^2/sec)

ℓ = dimensions of the scattering volume along the viewing axis (cm)

Using these expressions with the data obtained in our measurements we find

$$\sigma_{jk\ell}^{(meas)} = 1.32 \times 10^{-14}\ cm^2 \tag{21}$$

for the scattering channel 2170 Å → 2614 Å in lead vapor. This is to be compared to the calculated value (no quenching) shown in Table 4 of

$$\sigma_{jk\ell}^{(calc)} = 2.52 \times 10^{-14}\ cm^2 \tag{22}$$

We see that the calculated value compares fairly well with our measured value, being some 50% greater. All of the measurements reported herein were made on the 2170 Å → 2614 Å scattering channel, since this one is by far the most favorable in terms of a LIDAR system.

QUENCHING BY NITROGEN

The effect on the total scattering in the 2170 Å → 2614 Å channel, due to quenching by nitrogen and argon, was measured over a wide range of pressures. The quenching effects of argon were found to be negligible. All of the quenching measurements were made with very low lead densities in the scattering cell (~3×10^{10} cm^{-3}), to avoid self-trapping effects.

Figure 9 shows a quenching curve for 2614 Å radiation by N_2, in pure lead vapor, over the range of 1 to 5 torr. At high pressures (80–100 torr), the effects of Lorentz broadening become apparent and the quenching curve becomes quadratic. Extrapolation of the Stern-Volmer portion of the quenching curve to atmospheric pressure yields a quenching factor of

$$F_{k\ell}^{r} = 4.6 \times 10^{-3}$$

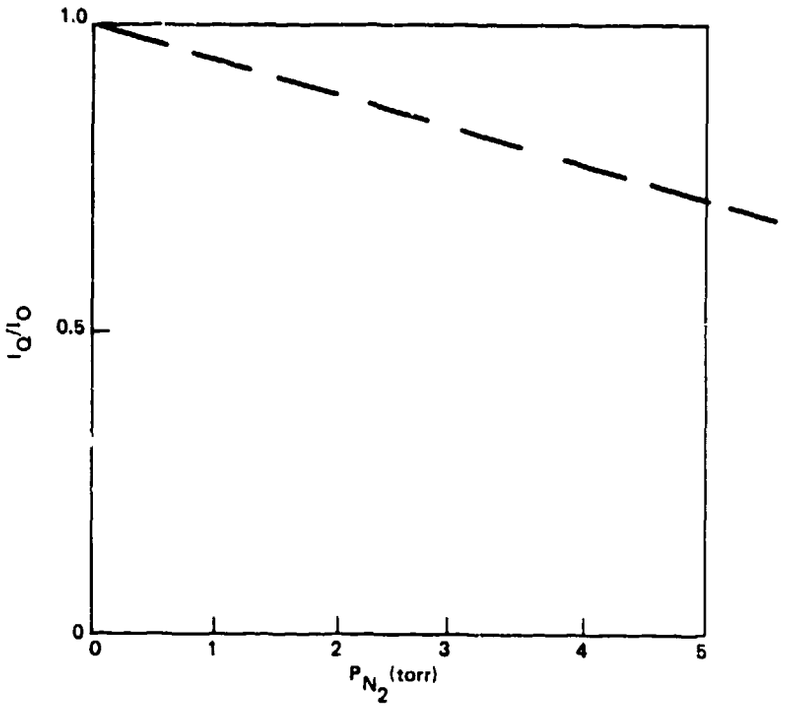

Figure 9. Quenching curve for N_2 on lead vapor.

as opposed to the estimated value shown in Table 4 of 4.2×10^{-2}. This discrepancy is not too surprising, since the estimated quenching was based on measured quenching cross section for the $7s^3P_1^o$ level, rather than the $6p6d^3D_1$ level for which no cross sections are available.

CONCLUSIONS

The results of the above measurements yield a total effective scattering cross section for the 2170 Å → 2614 Å channel in air, of

$$\sigma_{jk\ell}^{(meas)} = 6.1 \times 10^{-17}\ cm^2$$

as compared to the calculated value of 1.09×10^{-15} cm^2. The measured value is thus, roughly 18 times smaller than the estimated cross section obtained in Phase One of this project. Although the calculated cross section, exclusive of quenching, agrees fairly well with the measured value, the largest uncertainty in the Phase One calculations involved estimates of the appropriate quenching factors. Thus, the disparity noted above is not too surprising. Figure 10 shows an operational performance curve for a LIDAR system, operating in the 2179 Å → 2614 Å scattering channel of lead in the atmosphere, based on the measured cross section of 6.1×10^{-17} cm^2. The curve shows lead concentration vs SNR, for a range of 180 meters (~600 ft), utilizing the system parameters specified on page 13. Again, integration over 100 laser shots is assumed.

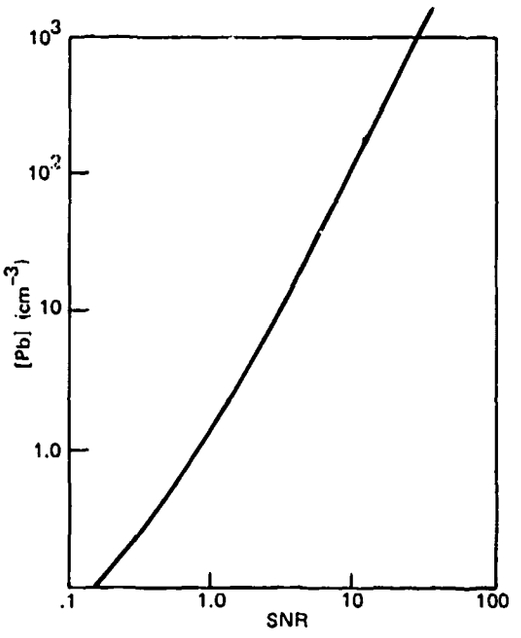

Figure 10. System performance characteristics for detection of lead at a range of 180 m and integration over 100 laser shots. Curve based on measured total effective scattering cross section.

An examination of the performance curve of Figure 10, indicates that a concentration of 100 cm^{-3} atomic lead could easily be detected at a range of 180 m (a SNR of 10). Although this represents a truly remarkable system sensitivity, this concentration level is roughly 100 times the expected background concentration of lead due to the natural decay of ^{222}Rn. In view of the fact that the proposed laser system specifications are already straining the present limits of technology, it is difficult to see where one could enhance the sensitivity by two orders of magnitude. Even operating at a range of 90 meters, overall system sensitivity is increased by slightly less than a factor of 10.

Although the results of this study indicate that a LIDAR system operating on the 2170 Å → 2614 Å scattering channel in lead would have extremely high sensitivity, it appears to fall short of the projected operational requirements by almost two orders of magnitude. Further, it would seem that a large technological investment would be required to make the system even marginally operational. Our conclusion must be, therefore, that a LIDAR remote detection system would not be feasible in the sensing of ^{222}Rn background daughter products.

REFERENCES

1. Solomon, JE and Silva, DM, "Detection of N_2^+ Produced by Ionizing Radiation in the Atmosphere", NUC TN-1497*, NOSC (Jan. 1975); Solomon, JE and Silva, DM, J. Appl. Phys. No. 47 (1976), p. 1519.

2. Schuler CJ, Pike CT, and Miranda HA, Appl. Optics, No. 10 (1971), p. 1689.

3. Hirschfeld T, Schildkrant ER, Tannenbaum H and Tannenbaum D, Appl. Phys. Lett., No. 22 (1973), p. 38.

4. Cunningham, PT and Link, JK, J. Opt. Soc. Amer., No. 57, (1967), p. 1000.

5. Svanberg, S, Phys. Scr., No. 5, (1972), p. 73.

6. Gibbs HM, Churchill GG, and Salamo EJ, Phys. Rev. A., No. 7, (1973), p. 1766.

7. De Zabra, RL and Marshall, Alan, Phys. Rev., No. 170, (1968), p. 28.

8. Lawrence, Gm, Astrophys. J., No. 148, (1967), p. 261.

9. Bates, DR and Damgaard, A, Phil. Trans. A., No. 242, (1949), p. 101.

10. Seaton, MJ, Royl. Astron. Soc. M.N., No. 118, (1958), p. 504; Burgess, A and Seaton, MJ, Royl. Astron. Soc. M.N., No. 120, (1960), p. 121.

11. Shore, BW and Menzel, DH, Principles of Atomic Spectra, (John Wiley and Sons, NY, 1968), n. pag.

12. Condon, EU and Shortley, GH, The Theory of Atomic Spectra, (Cambridge Univ. Press, 1964), n. pag.

13. Kirkbright, GF and Sargent, M, Atomic Absorption and Fluorescence Spectroscopy, (Academic Press, NY, 1974), n. pag.

14. O'Neil, R and Davison, G, Air Force Cambridge Research Laboratories Report, AFCRL-67-0277, (1967), n. pag.

15. Gibbs, HM, Phys Rev. A., No. 5, p. 2408.

16. Koller, LR, Ultraviolet Radiation, (John Wiley and Sons, NY, 1965), p. 191.

17. Smithsonian Physical Tables, n.p., n.d., p. 723.

*NOSC TNs are informal documents intended chiefly for internal use.